Local mechanical properties of human ascending thoracic aneurysms

Frances M. Davis, Yuanming Luo, Stéphane Avril, Ambroise Duprey, Jia Lu

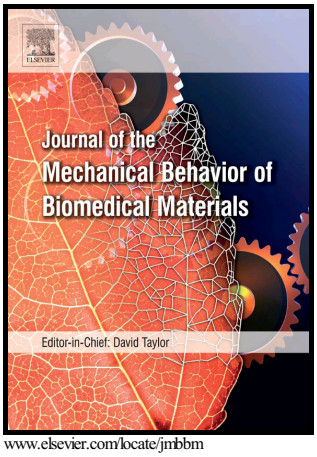

www.elsevier.com/locate/jmbbm

PII: S1751-6161(16)30045-5
DOI: http://dx.doi.org/10.1016/j.jmbbm.2016.03.025
Reference: JMBBM1858

To appear in: *Journal of the Mechanical Behavior of Biomedical Materials*

Received date: 1 June 2015
Revised date: 29 February 2016
Accepted date: 9 March 2016

Cite this article as: Frances M. Davis, Yuanming Luo, Stéphane Avril, Ambroise Duprey and Jia Lu, Local mechanical properties of human ascending thoraci aneurysms, *Journal of the Mechanical Behavior of Biomedical Materials* http://dx.doi.org/10.1016/j.jmbbm.2016.03.025

Local mechanical properties of human ascending thoracic aneurysms

Frances M. Davis[a,b,c,d,1,*], Yuanming Luo[e,1], Stéphane Avril[a,b,c], Ambroise Duprey[a,b,c,f], Jia Lu[e]

[a] *Ecole Nationale Supérieure des Mines de Saint-Etienne, CIS-EMSE, SAINBIOSE, F-42023 St. Étienne, France*
[b] *INSERM, U1059, F-42000 Saint Etienne, France*
[c] *Université de Lyon, SAINBIOSE, F-42000 Saint Etienne, France*
[d] *University of Southampton, Engineering Materials, SO17 1BJ, Southampton UK*
[e] *Department of Mechanical and Industrial Engineering, The University of Iowa, Iowa City, IA*
[f] *Cardiovascular Surgery Service, CHU de Saint-Etienne, F-42055 St. Étienne CEDEX 2, France*

Abstract

Ascending thoracic aortic aneurysms (ATAAs) are focal, asymmetric dilatations of the aortic wall which are prone to rupture. To identify potential rupture locations in advance, it is necessary to consider the inhomogeneity of the ATAA at the millimeter scale. Towards this end, we have developed a combined experimental and computational approach using bulge inflation tests, digital image correlation (DIC), and an inverse membrane approach to characterize the pointwise stress, strain, and hyperelastic properties of the ATAA. Using this approach, the pointwise hyperelastic material properties were identified on 10 human ATAA samples collected from patients undergoing elective surgery to replace their ATAAs with a graft. Our method was able to capture the varying levels of heterogeneity in the ATAA from regional to local. It was shown for the first time that the material properties in the ATAA are unmistakably heterogeneous at length scales between 1 mm and 1 cm, which are length scales where vascular tissue is typically treated as homogeneous. The distributions of the material properties for each patient were also examined to study the inter- and intra-patient variability. Large inter-subject variability was observed in the elastic properties.

Keywords: thoracic aneurysm, heterogeneous material properties, inverse elastostatic analysis, intra-patient variation, inter-patient variation, distribution of material properties

1. Introduction

Ascending thoracic aortic aneurysms (ATAAs) are focal, asymmetric dilatations of the aortic wall. A serious life-threatening pathology, the incidence of ATAAs is estimated at 10.4 per 100,000 people, suggesting that approximately 45,000 cases are diagnosed each year in Europe and the United States [8]. If an ATAA spontaneously ruptures, the result is almost invariably death [18]. Only two options exist for treating ATAAs: preemptive surgery or surveillance. Hence, the current objective in aneurysm care is to prevent rupture. Surgical repair is only indicated when the diameter of the aneurysm exceeds 5.5 cm. However, aneurysms with diameters greater than the surgical threshold may remain stable [1, 3, 18] and conversely, small aneurysms ($<$ 4.5 cm) do rupture [1, 4, 18]. Rupture is a localized phenomenon and to identify potential rupture locations in advance, one must consider the local mechanical conditions of the tissue.

ATAAs are evolving structures; both the geometry and the tissue properties change as the aneurysm grows. Existing studies showed a significant increase in matrix metalloproteinase activity [20] and apoptosis of smooth muscle cells in thoracic aneurysms [31]. Well-developed aneurysms typically have an attenuated media, fragmented elastin fibers, and abnormal collagen networks [17, 31]. Since the the local remodeling

*Corresponding author
Email addresses: frances.davis@emse.fr (Frances M. Davis), yuanming-luo@uiowa.edu (Yuanming Luo), avril@emse.fr (Stéphane Avril), ambroise.duprey@emse.fr (Ambroise Duprey), jia-lu@uiowa.edu (Jia Lu)
[1] Co-first authors

history dictates the tissue properties, the spatial distribution of mechanical properties is expected to be heterogeneous. Thus, our understanding of aneurysm mechanics and mechanobiology is incomplete without detailed knowledge of the heterogeneous properties.

Presently, ATAA properties were characterized at a length scale of approximately 2 centimeters, a scale we call regional. A few authors have attempted to characterize the regional variation in mechanical properties of the ATAA [2, 16, 19]. Uniaxial tensile tests on ATAA specimens have indicated that the mechanical properties vary regionally [2]. The observation of a regional variation in the mechanical properties confirms the hypothesis that the degradation of the properties in the ATAA is localized rather than uniform [34]. To address the issue of the inhomogeneity of the ATAA, particularly when attempting to identify potential rupture conditions, it is necessary to consider the variation in mechanical properties at the millimeter scale [25, 26, 37].

The authors have previously presented a technique combining inverse membrane analysis, digital image correlation (DIC), and bulge inflation tests capable of identifying the heterogeneous elastic properties of planar soft tissues [5]. This technique enables the identification of heterogeneous properties to a sub-millimeter scale. The local wall tension is calculated from the membrane equilibrium equations and the local strain is calculated using DIC. The local elastic properties of any membrane structure can be identified by fitting a constitutive model to the local stress-strain response. In this manuscript, the same method was implemented to identify the local material properties of human ATAAs. Using DIC , full-field deformation data as a function of pressure up to rupture was obtained. The pressure and deformation data were used as inputs to the inverse membrane analysis which calculated the wall tension in the ATAA. The acquired full-field wall tension and strain data were fitted to the Gasser-Ogden-Holzapfel (GOH) constitutive model [9] to identify the local material properties. The local values of the GOH model parameters were then examined to quantify the degree of intra- and inter-patient variability. Maps of the local strain energy were also created, consolidating the GOH model parameters down to a single parameter, to quantify the degree of heterogeneity in the local material properties.

2. Methods

2.1. Pointwise parameter identification

Six ATAA sections were collected from patients undergoing elective surgery to replace their ATAAs with graft in accordance with a protocol approved by the Institutional Review Board of the University Hospital Center of St. Etienne. Information on each of the patients' age, gender, and aneurysm diameter (as measured during a pre-surgical CT scan) are shown in Table 1. A total of 10 samples were tested according to our previously developed protocol for identifying the pointwise distribution of the mechanical properties of soft tissues using bulge inflation tests [5]. The method described in our previous paper [5] is briefly outlined for completeness.

Square samples approximately 4 cm x 4 cm were clamped to an inflation device. The samples were inflated using a syringe pump system where water was infused at a constant rate. During the test, images of the deforming sample surface were collected every 3 kPa until the sample ruptured. After rupture, the collected images were analyzed using the commercial correlation software ARAMIS (GOM, v. 6.2.0) to determine the three dimensional displacement of the tissue surface. A deforming NURBS mesh was created from the DIC point clouds. The surface right Cauchy-Green tensor, $\mathbf{C}$, and surface Green-Lagrange strains, $\mathbf{E}$, were computed from the identified displacements using the local coordinate system of the NURBS mesh. The Cauchy membrane tension, $\mathbf{t}$, at every Gauss point in the NURBS mesh was identified using an inverse membrane approach [5, 22] which formulates the equilibrium problem directly on the deformed configuration. Additional details on the calculation of the surface strains and wall tension with respect to the NURBS coordinates can be found in [5].

After identifying the wall tension and strain at each Gauss point in the mesh, the data were fitted to a modified form of the GOH model [9, 14, 30]:

$$w = \frac{\mu_1}{2}\left(\mathrm{I}_1 - \ln\left(\mathrm{I}_2\right) - 2\right) + \frac{\mu_2}{4\gamma}\left(\mathrm{e}^{\gamma\left(\mathrm{I}_\kappa - 1\right)^2} - 1\right) \tag{1}$$

where $I_1 = \mathrm{tr}(\mathbf{C})$, $I_2 = \det(\mathbf{C})$, and $I_\kappa = \mathbf{C} : (\kappa \mathbf{I} + (1 - 2\kappa)\, \mathbf{M} \otimes \mathbf{M})$. In Eq. 1, the first term accounts for the isotropic behavior of the matrix which includes the ground substance and elastin fibers while the second term represents the contribution of the collagen fiber network. The response of the matrix is modeled using a two-dimensional neo-Hookean model. Note that a term containing I_2 is necessary to ensure that the two-dimensional stress behavior mimics the response of a three-dimensional incompressible neo-Hookean solid. The parameters μ_1 and μ_2 describe the stiffness of the matrix and the stiffness collagen fibers, respectively. Both parameters have units of force per unit length. The model parameter, γ, describes the strain stiffening behavior of the collagen fibers. Higher values of γ indicate that the mechanical response of the collagen fibers stiffens at lower stretches. Two additional parameters are necessary to describe the collagen fiber orientation, a unit vector, $\mathbf{M} = \sin\theta\, \mathbf{E}_1 + \cos\theta\, \mathbf{E}_2$, in the preferred fiber direction and the dispersion of collagen fiber orientation, κ. When all of the collagen fibers are aligned in the preferred fiber direction, $\kappa = 0$, and when the fibers are randomly oriented, $\kappa = 0.5$. The model parameters were constrained such that: μ_1, μ_2, $\gamma \geq 0$, $0 \leq \theta \leq \pi$, and $0 \leq \kappa \leq 0.5$. At each Gauss point in the mesh, the local model parameters were identified by minimizing the difference between the wall tension derived from the surface strain energy function (Eq. 1) and the wall tension computed from the inverse analysis. To verify that the set of identified material parameters was unique, the initial values used in the minimization routine were varied. Since the same set of material parameters were obtained independent of the initial guess, the identified parameters were assumed to be unique. Note that the GOH model, given in Eq. 1, was only selected after attempting to fit the data with simpler constitutive models such as the neo-Hookean or Demiray's model [6].

2.2. Statistical analysis

For each bulge inflation test the values of the material parameters, μ_1, μ_2, γ, κ, θ, were identified at approximately 2000 locations. To compare the intra- and inter-specimen variability in the material parameters, histograms of μ_1, μ_2, γ, κ, θ were generated for every sample. In addition to the histograms, the mean, median, standard deviation, skewness, and kurtosis for each parameter and every test were computed. The mean and median describe the central tendency of the distribution. Skewness is a measure of whether the distribution is symmetric about its mean. The standard deviation and the kurtosis both quantify the dispersion in the data.

3. Results

3.1. Validity of the reconstruction

Using a technique described previously [5], the average distance deviation between the measured DIC point clouds and the constructed NURBS meshes were computed. The precision of the geometric reconstruction is critical since, for a membrane, the wall tension depends only on the load and the deformed geometry. As expected, the NURBS meshes for each sample were able to faithfully capture the geometry. The maximum distance deviation across all of the samples was 80 μm.

To ensure that the membrane assumption could be used to reconstruct the local stresses a computational study was completed to identify the limiting ratio of the out-of-plane displacement to specimen diameter (Fig. 10). At values below the limiting ratio of 0.2, the error on the stress reconstructed with the membrane assumption is greater then 15%. The details of how the limiting ratio was calculated can be found in the Appendix. Using the collected DIC point clouds, the ratio of the diameter to the out-of-plane displacement can be calculated for every specimen. For all the tested samples, the value was greater than the 0.2 limit at an inflation pressure of 15 kPa.

3.2. Local stress-strain behavior

In Fig. 1, the magnitude of the wall tension and strain at pressures of 15, 30, and 39 kPa for Patient 3a are shown. Note that, in terms of the stress it induces, the pressure applied in the test is not equivalent to a blood pressure due to the new shape of the specimen. The highest value of the wall tension in Fig. 1a, c, and e occurs in the upper right hand corner of the sample. But, this high value in the wall tension is due to the boundary conditions applied in the inverse membrane simulation. Ignoring these values, the peak wall

tension occurs at the apex of the sample. For all of the samples tested the peak wall tension was located at the sample's apex when the spurious boundary values were ignored.

The strain localized in three locations very early in the test (Fig. 1b). The pattern of strain concentrations remained the same throughout the test with the magnitude of the strain simply increasing with increasing pressure. As indicated in Fig. 1f with a black circle, rupture occurred at one of these strain concentrations. While the pattern of strain concentrations changed from sample to sample, the strain localizations always happened very early in the test and remained largely unchanged until rupture. Moreover, rupture initiated in one the observed strain concentrations in every test.

Using the local values of strain and wall tension at each pressure increment, curves of the local material response were created. To facilitate plotting the local wall tension vs stretch curves, the eigenvalues, λ_α^2 , and eigenvectors, $\mathbf{u}^{(\alpha)}$, of the surface right Cauchy-Green tensor, $\mathbf{C}$, were identified. The principal stretches, λ_α, were found by taking the square root of the eigenvalues of $\mathbf{C}$. The second Piola-Kirchoff wall tension, $\mathbf{s}$, was rotated into the axes of principal stretch using $\mathbf{u}^{(\alpha)}$, the eigenvectors of $\mathbf{C}$. In Fig. 2, four individual curves of the rotated Cauchy wall tension vs the principal stretches (λ_1 and λ_2) are plotted. All of the curves display the non-linear behavior that is common in vascular tissues although the degree of nonlinearity varied. Each location also experienced a slightly different loading path. The loading path pictured in Fig. 2d is almost equi-biaxial in contrast there is a pronounced asymmetry in ratio of $\lambda_1 : \lambda_2$ in Fig. 2a.

The maximum and mean values of the magnitude of the Cauchy wall tension and the magnitude of the Green-Lagrange strain at the pressure just preceding rupture are listed in Table 2. Although the maximum wall tension varied significantly from patient to patient, the maximum strain at failure appeared to be clustered around 0.3 for Patients 1-5. The significantly higher strain to failure for Patient 6 may be due to the large age difference between Patient 6 (age = 55 yrs) and the remainder of the cohort (mean age = 76.6 yrs).

3.3. Pointwise material properties

For the bulge inflation tests performed in this study, clamps with smooth rounded edges were used. This clamping technique produced a fixed boundary condition at the edge of the clamps, inducing bending and transverse shear stress. However, these stresses are expected to decay so rapidly that they need not be considered in regions a short distance away from the boundary. To minimize the influence of the mechanical boundary, only the center region of each sample was analyzed in the inverse analysis, discarding data within 5 mm of the clamp edge. In the inverse stress computation, the boundary of the analysis domain was fixed. Enforcing displacement based boundary conditions also causes a boundary layer effect whereby the stress solution near the boundary is expected to be inaccurate [21, 22]. To minimize the influence of this boundary layer on the material property identification, the outer ring of elements were excluded from the material parameter identification and any further analysis. By retrospective comparison with the forward finite element analysis, described in the Appendix, the size of the boundary region was confirmed for each specimen.

The local wall tension vs stretch curves at points outside of the boundary region were then used to compute the local model parameters μ_1, μ_2, γ, κ, and θ. In Fig. 2, the model fits for four representative curves are presented. The GOH model was able to capture the variety of nonlinear responses observed in Fig. 2 well ($R^2 = 0.99$). The average R^2 values were calculated for each sample and ranged from 0.96 to 0.99.

Maps of the material properties for Patient 1 are presented in Figs. 3 - 4. For all of the material parameters the spatial changes occur gradually. As expected, for both samples the values of μ_2 are an order of magnitude greater than μ_1, reflecting the difference in stiffness between the collagen fibers and the matrix. For both samples, the values of κ are significantly skewed toward 0.5 suggesting that the collagen fibers are distributed over wide range of angles approaching an isotropic orientation. The preferred fiber direction, $\mathbf{M}$ is described by a single parameter, the preferred fiber angle, θ, which is measured counterclockwise from the horizontal grid lines. A preferred fiber direction of 0 or 180° corresponds to the circumferential direction *in vivo*. While the spatial distribution of the parameters in Figs. 3 - 4 are very different, the range of the values are similar except for the preferred fiber angle, θ. The values of θ for Patient 1a span the full range of

possible angles with a large portion oriented at 180° while in Patient 1b the fiber angle only varies between 0 and 35°.

To examine the combined effect of all 5 model parameters, the value of the strain energy for an equi-biaxial stretch, $\lambda = 1.2$, was calculated using Eq. 1. In this way, a single parameter, the strain energy, can be used to evaluate the differences between samples and between locations within the same sample. Figure 5 shows the strain energy maps for Patients 1 and 4. For all of the samples, the strain energy pattern is clearly heterogeneous. The dark red areas show regions where the most strain energy was stored for each sample. Since a uniform deformation was assumed to calculate the strain energy, these dark red areas are the stiffest regions in the sample. In Fig. 5a, the maximum value of the strain energy is almost quadruple the maximum value in Fig. 5b. Conversely, the values of the strain energy over most of the sample in Fig. 5c and d are approximately the same. In both cases, there are significant variations in the strain energy over the sample providing evidence that the behavior of the ATAA is truly heterogeneous.

3.4. Distribution of the parameters

Histograms of the pointwise model parameters were generated for Patients 1, 3, 4, and 6 to examine intra-patient variability. In Fig. 6, the histograms of μ_1, μ_2, γ, κ, and θ for the two samples from Patient 6 are plotted. The values of μ_1 in Fig. 6a are significantly skewed towards zero for both samples. The values of μ_1 were less than 0.01 N/mm at more than 50% of the locations where the properties were identified. While the distributions are similar, for Patient 6b the tail of the distribution is longer with a greater number of points with values larger than 0.02 N/mm. For μ_2 and γ, the data in both cases are tightly clustered around their means with slightly more outliers towards the high end of the distribution. The values of κ are strongly skewed towards its maximum value of 0.5. In addition to the large cluster of points between 0.4 and 0.5, there is also a long tail stretching towards zero. In contrast to the other parameters, the distribution for the preferred fiber angle, θ, is almost flat. For Patient 6a, small peaks occur at 0-20° and again at 160 -180°. For Patient 6b, only one small peak occurs at 90°.

A two-sample Kolmongorov-Smirnov test was used to test the null hypothesis that the distributions for the material parameters from Patient 6a were from the same continuous distribution as Patient 6b. The null hypothesis was rejected at the 10% significance level. The two-sample Kolmongorov-Smirnov test was run separately for each model parameter. For all of the parameters, the null hypothesis was rejected; while the distributions appear similar, they cannot be approximated with a single probability distribution function. This process was repeated for the material property distributions from Patients 1, 3, and 4. Again, the null hypothesis was rejected for all of the material property distributions from Patients 1, 3, and 4.

To examine inter-patient variability, 41 sets of histograms comparing the properties between the patients were created. Figure 7 shows one representative set of histograms comparing the properties identified for Patient 1b and Patient 4b.These two samples were selected to illustrate how pronounced the differences in material parameters between two patients can be. The distribution of values for μ_1 in Fig. 7a for Patient 1b and Patient 4b are very similar to one another, and indeed, to the distribution in Fig. 6a. The values of μ_2 for Patient 1b and 4b cover different ranges with a slight overlap between the upper end of the distribution for Patient 1b and the lower end of the distribution for Patient 4b. In spite of the fact that the ranges are different, the shape of the distributions are similar, both exhibiting long tails at the high end of the distribution. In comparison to Fig. 6c, the values for γ in Fig. 7c cover a wide range. The values of γ in Fig. 6c extend from 0.5 to 5 while in Fig. 7c the value of γ varies from 2 to almost 40. The higher values of γ indicate that the mechanical response begins to stiffen at lower strains. In Fig. 7, both of the κ distributions only cover the range between 0.3 and 0.5. Although the range for both distributions is the same, the values of κ for Patient 4b are clearly shifted more towards 0.5, the maximum value of κ. In fact, the κ distribution for Patient 1b is the only one where the distribution is not severely skewed to the right of its mean. Unlike those in Fig. 6d these κ distributions lack a long tail stretching towards zero. For Patient 4b, the distribution for the preferred fiber angle, θ, is flat resembling those seen in Fig. 6e. Patient 1b has a markedly different distribution with a predominant preferred fiber direction of approximately 20°.

The measures given in Table 3 quantify the shapes of the histograms shown in Figs. 6 and 7. These same measures are reported for the other samples tested in the Appendix in Table 5. If the data can be modeled with a normal distribution the mean and median will have similar values. The standard deviation

quantifies the amount of variation in the data, where values approaching zero indicate the data points fall close to the mean. For a symmetric data set, the skewness will be nearly zero. When the majority of values occur at the low end of the distribution the skewness is positive and when the majority of the values occur at the high-end of the distribution the skewness is negative. Kurtosis is a measure of whether a distribution is flat or peaked when compared with a normal distribution. For a normal distribution, the kurtosis is 3. For a uniform (flat) distribution, the kurtosis will be 0.

Data that can be approximated with a normal distribution, can be described with only two parameters: the mean and the standard deviation. To determine if any of the material parameters can be well-modeled using a normal distribution the Anderson-Darling test was used. The null hypothesis that the material property data is from a population with a normal distribution was rejected at a significance level of 10%. For every sample and every model parameter, the null hypothesis was rejected.

4. Discussion

In this manuscript, we have identified the pointwise heterogeneous distribution of material properties of 10 human ATAA samples. The local properties were determined using our previously developed experimental protocol [5] which exploits the assumption that the ATAA can be modeled as a membrane. While the feasibility of the protocol was demonstrated in [5], this manuscript is the first time that the method was used to characterize the mechanical properties for a patient cohort. The property distributions in Figs. 3, 4, and 5 show that ATAAs are highly heterogeneous. This is particularly significant in light of the fact that this considerable level of property variation was observed in small samples ($d = 3$ cm), the length scale where vascular tissue is typically treated as homogeneous. In addition, statistical tests revealed that the mechanical properties do not follow a normal distribution and confirmed that the multiple samples taken from the same patient display a degree of regional and local heterogeneity.

Since the experimental protocol used DIC to obtain full-field displacement measurements, it was possible to compute the strain locally. The local strain maps (Fig. 1 d-f) consistently revealed strain localizing in the rupture region preceding failure, confirming the observations reported in [26]. Dynamic-CT scans collected prior to surgery were used to create patient-specific finite element models for Patients 2, 4, 5, and 6 [33]. The results show that the wall tensions and strains observed at rupture exceed those expected *in vivo*. Consequently, the wall tensions and strains at higher pressures (Fig. 1 c,f) capture the response of the ATAA to supra-physiological loads.

In this study, the ATAA is modeled as a membrane. Membrane structures are particularly interesting because they are statically determinate. When the deformed configuration of a membrane structure and the corresponding loads and boundary conditions are given, the wall stress is completely determined by the equilibrium equations. This enables the tress field to be computed directly without the consideration of the membranes mechanical properties [21, 23, 26, 36]. Miller and Lu [23] have discussed in depth this type of inverse problem for statically determinate structures, specifically using the membrane assumption to predict the wall stress in intracranial aneurysms. The membrane assumption requires the thickness of the ATAA wall to be small relative to its radius of curvature. In this study, the membrane assumption is validated using a computational procedure described in the Appendix.

The material properties in the ATAA are unmistakably heterogeneous. Figures 3 and 4 illustrate how these properties vary over the face of the aneurysm. Previous studies have found that the mechanical properties of the ATAA vary regionally with the inner curvature of the aneurysm being the least stiff [2, 7, 17]. As shown in Fig. 8, the two samples from Patient 1 were both taken from locations adjacent to the inner curvature of the aneurysm. Using the terminology from Choudhury et al. [2], Samples 1a and 1b came from the posterior and anterior regions of the aneurysm, respectively. The central sample in Fig. 8 was tested but slipped in the bulge inflation device before it ruptured. In agreement with the results presented in [2], the posterior sample (1a) was stiffer than the anterior sample (1b) (Fig. 5a-b). The two samples from Patient 4 were taken from the anterior and the outer curvature of the aneurysm for Patient 4a and 4b, respectively. The results of Choudhury et al. [2] would predict that Patient 4b would be stiffer than 4a which is consistent with the results in Fig. 5c-d. In fact this regional variation in mechanical properties explains why the two-sample Kolmongorov-Smirnov test found that none of the

intra-patient samples could be described with a single distribution function (Fig. 6). Together the results point to two levels of heterogeneity: regional ($2-3$ cm) and local ($0.3-0.4$ mm). Unfortunately, this detailed information on the location of the tested samples was not recorded for Patients 3 and 6 making the local spatial heterogeneity more difficult to interpret.

The GOH model was used to describe the nonlinear response of the ATAA (Fig. 2). The parameters were identified by considering the entirety of all three wall tension vs stretch curves and determining the five parameters simultaneously. Although not clear from Figs. 6 and 7 at more than 25% of the points used to identify the parameters the value of μ_1 was equal to 0. While the matrix is expected to be much softer than the collagen fibers, finding $\mu_1 = 0$ is unrealistic and suggests that the elastin fibers and ground substance do not contribute to the overall mechanical response. Other investigators have corrected this problem by assigning a relationship between μ_1 and μ_2 [13] or by separately fitting the low strain region of the stress-strain curve using only the contribution of the matrix to the stress [32]. Since fixing the relationship between μ_1 and μ_2 would make it impossible to examine the spatial patterns in μ_1 or μ_2 the latter solution would be more suited to our approach. For a small data set, the transition between low strain and high strain is identified by manually inspecting the curves and selecting a window that is appropriate for the data collected [32]. However, in our case, due to the abundance of data and the variety of loading regimes (Fig. 2), this process could not be implemented robustly. Instead, to verify that the pointwise materials properties were properly identified specimen specific finite element analyses were run for every sample tested. The method, described previously in [5], is briefly detailed in the Appendix for completeness. The wall tensions and strains predicted by the forward simulation accurately replicate not only the global deformation but also the local stress and strain patterns. The simulation results provide compelling evidence that although the values for μ_1 may not be realistic from a microstrucutral perspective they do accurately capture the tissue response.

In the GOH model two parameters are used to describe the collagen fiber orientation: κ, the fiber dispersion and θ, the preferred fiber angle. The model assumes a planar symmetric fiber distribution about the preferred (mean) fiber angle, θ [28]. The dispersion parameter κ varies from 0 to $\frac{1}{2}$ with $\kappa = 0$ corresponding to a perfect alignment of collagen fibers and $\kappa = \frac{1}{2}$ indicating isotropy. The preferred fiber angle becomes less influential as the κ approaches 0.5, since, for an isotropic arrangement of fibers there is no preferred direction. As shown in Figs. 6 and 7, the values of κ are skewed with the majority of values falling between 0.35 and 0.50. Similar behavior was observed in all of the tested samples. Although the flat distribution of θ (Fig. 6 and 7) together with the high values of κ ($0.35 \leq \kappa \leq 0.5$) suggest that there is no prominent fiber direction at the sample scale, the local orientation of the preferred fiber direction does vary significantly from point to point.

Not surprisingly the ATAAs exhibited large inter-subject variability in the elastic properties. The youngest patient, Patient 6, had the highest strains to failure (Table 2) and displayed the least stiff response (Fig. 6, Table 3 and 5). This is in agreement with the the existing literature on the effect of aging [10–12, 29] which found that the healthy thoracic aorta stiffened progressively with age with substantial stiffening occurring between patients aged 30-60 and those over the age of 60. At 55 years old, Patient 6 would be in the younger group while the remainder of the cohort had a mean age of 76.6 yrs.

This manuscript has focused on describing the local material parameters. However the analysis of the material property distributions largely ignored the spatial position where the values were identified. In the future, the data must be reanalyzed to determine how the inclusion of spatial position would influence the results with a particular emphasis on the location where rupture initiates. The hope is that the spatial trends in the data will make it possible to identify the origin of the spatial heterogeneity in the material properties. For example, the pronounced heterogeneity in the properties may be the result of mechanobiological dysfunction [15]. Due to the dysfunction, the tissues loses its mechanosensitivity leading to an impaired adaptation of the local mechanical properties. If mechnobiological dysfunction initiates and drives the growth of thoracic aneurysm, then the spatial heterogeneity observed in this study would be unique to aneurysms. New findings on the origin of spatial heterogeneity and its link to aneurysm growth and formation could open the way for region-specific therapies to restore the structural integrity of the aneurismal aorta.

There are, however, several limitations to our work. First and foremost, this method is only applicable to

membranes. A membrane must have negligible bending resistance and a thickness that is small compared to the other dimensions. At low pressures ($p < 15$ kPa), the membrane assumption may be compromised since the specimen is only slightly inflated and the ratio of the out-of-plane displacement to specimen diameter is small (Fig. 10). At low pressures bending is also the dominant mode of deformation, again compromising the reliability to the membrane assumption. For this reason the low pressure response has been eliminated from Fig. 2. As a result, the stretches start at approximately 1.1 where the ratio of the out-of-plane displacement to specimen diameter if greater than 0.2. The details of how the limiting ratio was calculated can be found in the Appendix. The membrane assumption has also led us to model the ATAA as a monolayer. The wall of the ATAA is composed of three distinct layers: the intima, media, and adventitia; but in modeling the ATAA as a membrane, we have disregarded this structural information. The resulting material parameters are therefore representative of the combined response of the three layers.

Second, the wall tension was reported instead of the stress. The stress cannot be directly computed without knowledge of the local thickness of every element. As a result, only two-dimensional stiffness properties, μ_1 and μ_2, were reported to describe the material response instead of the modulus type parameters computed in three-dimensional constitutive models. Accurately measuring the local thickness of an ATAA is difficult and inexact thickness values would only compromise the stress calculations [24]. If a technique for precisely identifying the local thickness could be found, it would be interesting to investigate if there is any relationship between the thinnest sections of tissue and the locations of strain concentrations (Fig. 1).

Finally, there were only a small number of specimens tested limiting our ability to throughly compare the influence of sex and age. There did not appear to be a large difference in parameters between the male (Patients 2, 3, and 4) and female (Patients 1 and 5) patients but this would need to be confirmed with a much larger cohort of patients. Likewise since there was only one "young" patient tested in this study and the trends observed with respect to age must be confirmed. The absence of healthy (non-aneurysmal) age-matched controls makes it impossible to determine if the heterogeneity observed in these aneurysms is related to aneurysm growth, occurs naturally due to aging, or is present even in young healthy arteries. Additional experimental studies which include healthy and aneurysmal tissue are needed to explore the relationship between the identified heterogeneous material properties, aneurysm growth, and aging.

In summary, the pointwise material properties of 10 human ATAA samples were identified in this study. Our method was able to capture the varying levels of heterogeneity in the ATAA from regional to local. The distributions of the material properties for each patient were examined to study the inter- and intra-patient variability. Future studies on the heterogeneous properties of the ATAA would benefit from some form of local structural analysis such as histology or multi-photon microscopy. The structural data and knowledge of the spatial trends should provide the information necessary to move from merely measuring the local material properties to uncovering the links that exist between the underlying microstructure and local properties.

Acknowledgments

This work was supported in part by The University of Iowa Mathematical and Physical Sciences Funding Program. Dr. Davis was supported by the Whitaker International Scholars Program.

Appendix

Membrane assumption validation

To validate the membrane assumption, a bulge inflation test was simulated in ABAQUS (v. 6.9) to emulate the experiments at low pressures, where the membrane assumption is most likely to be compromised. Two meshes of circular plate were created. In the first model, the plate had a thickness of 2.40 mm, which is slightly larger than the thickest specimen tested (t=2.38 mm). In the second model, the plate was given a thickness of 2 mm, representing the average thickness of the specimens tested in this study. The diameter of the plate, 30 mm, matches the size of the clamped area during inflation test. The plate was meshed using continuum shell elements (SC8R) with 2 layers of elements through the thickness and a total of 2970 nodes

and 1882 elements. The perimeter nodes on the mid-plane were fixed (Fig. 9), to mimic the experimental constraint. The material was modeled using a neo-Hookean function (c_{10}= 0.04 MPa, D_1= 0). Four different levels of pressure, which produced a range of deformation comparable to the experimental displacement at the low pressure end, were considered. The deformed configurations from the ABAQUS analysis were used as inputs to inverse membrane analysis. The ABAQUS stress fields were used as the reference for comparison with the inverse membrane solution. As in the actual experiments, only the center region of 20 mm in diameter was extracted and used in the inverse analysis (Fig. 9(b)).

The principal components of the wall tensions (N/mm) were computed from ABAQUS and the inverse approach. Since the ABAQUS model utilized a continuum shell element, the tension was computed by averaging the in-plane stress over the thickness and multiplying the result by the current shell thickness. The difference between the ABAQUS results and the inverse predictions at four levels of deformation for the first principal tension is plotted in Fig. 10. Clearly the error decreases rapidly with the deformation. Experimentally at 15 kPa, the maximum out-of-plane displacement, H, was roughly 4 mm, giving a H/L ratio of 0.2. From Fig. 10, this likely results in a stress error of approximately 12%. The error decreases to approximately 5% at 5 mm of deformation. To put this into perspective, the average maximum deformation for the samples tested was 5.7 mm. Keeping in mind that the material parameter identification is primarily driven by the high pressures states, these results suggest that the membrane assumption is a reasonable approximation for computing stresses.

Forward Validation

To verify that the material properties had been properly identified, a forward finite element validation was performed simulating the inflation experiment. The heterogeneous material properties calculated at each Gauss point were mapped back the NURBS mesh. Then the pressure was increased until the rupture pressure was reached. The magnitude of the displacement, strain, and wall tension from the forward validation were compared to the experimental results. Previous studies have shown that the error tends to plateau at pressures above 30 kPa [5]. In light of this, Table 4 presents the average percent error at the highest pressure stage for each case. Figure 11 shows the spatial distribution of the error for the magnitude of the displacement, strain, and wall tension at three different pressures for Patient 1a. As the pressure level increases the error between the experimental data and the forward predictions decreases. As expected, there is a significant decrease between 15 and 45 kPa but between 45 and 57 kPa the error stabilizes. The stress errors are around 2-5%, consistent with the results of the membrane validation. Note that the errors in displacement are much smaller than the errors in strain or stress. The errors in the displacement calculation are propagated into the strain and then stress calculation; therefore the displacement errors must be very small to ensure that accurate strains and stresses are calculated.

References

[1] Chau, K.H., Elefteriades, J.A.: Natural history of thoracic aortic aneurysms: size matters, plus moving beyond size. Progress in cardiovascular diseases **56**(1), 74–80 (2013). DOI: 10.1016/j.pcad.2013.05.007.

[2] Choudhury, N., Bouchot, O., Rouleau, L., Tremblay, D., Cartier, R., Butany, J., Mongrain, R., Leask, R.L.: Local mechanical and structural properties of healthy and diseased human ascending aorta tissue. Cardiovascular Pathology **18**(2), 83–91 (2009). DOI: 10.1016/j.carpath.2008.01.001.

[3] Coady, M.A., Rizzo, J.A., Hammond, G.L., Mandapati, D., Darr, U., Kopf, G.S., Elefteriades, J.A.: What is the appropriate size criterion for resection of thoracic aortic aneurysms? The Journal of thoracic and cardiovascular surgery **113**(3), 476–91 (1997). DOI: http://dx.doi.org/10.1016/S0022-5223(97)70360-X.

[4] Davies, R.R., Goldstein, L.J., Coady, M.A., Tittle, S.L., Rizzo, J.A., Kopf, G.S., Elefteriades, J.A.: Yearly Rupture or Dissection Rates for Thoracic Aortic Aneurysms : Simple Prediction Based on Size. Annals of Thoracic Surgery **73**, 17–28 (2002)

[5] Davis, F.M., Luo, Y., Avril, S., Duprey, A., Lu, J.: Pointwise characterization of the elastic properties of planar soft tissues: application to ascending thoracic aneurysms. Biomechanics and Modeling in Mechanobiology (2015). DOI: 10.1007/s10237-014-0646-9.

[6] Demiray, H.: A note on the elasticity of soft biological tissues. Journal of Biomechanics **5**, 309–311 (1972)

[7] Duprey, A., Khanafer, K., Schlicht, M., Avril, S., Williams, D., Berguer, R.: In Vitro Characterisation of Physiological and Maximum Elastic Modulus of Ascending Thoracic Aortic Aneurysms Using Uniaxial Tensile Testing. European Journal of Vascular & Endovascular Surgery **39**(6), 700–707 (2010). DOI: 10.1016/j.ejvs.2010.02.015.

[8] Elefteriades, J.A., Farkas, E.A.: Thoracic aortic aneurysm clinically pertinent controversies and uncertainties. Journal of the American College of Cardiology **55**(9), 841–57 (2010). DOI: 10.1016/j.jacc.2009.08.084.

[9] Gasser, T.C., Ogden, R.W., Holzapfel, G.a.: Hyperelastic modelling of arterial layers with distributed collagen fibre orientations. Journal of the Royal Society, Interface **3**(6), 15–35 (2006). DOI: 10.1098/rsif.2005.0073.

[10] Groenink, M., Langerak, S.E., Vanbavel, E., van der Wall, E.E., Mulder, B.J.M., van der Wal, A.C., Spaan, J.A.: The influence of aging and aortic stiffness on permanent dilation and breaking stress of the thoracic descending aorta. Cardiovasular Research **43**, 471–480 (1999)

[11] Guinea, G.V., Atienza, J.M., Rojo, F.J., Garcia-Herrera, C., Yiqun, L., Claes, E., Goicolea, F.J., Elices, M.: Factors influencing the mechanical behaviour of healthy human descending thoracic aorta. Physiological Measurement **31**, 1553–1565 (2010). DOI: 10.1088/0967-3334/31/12/001

[12] Haskett, D., Johnson, G., Zhou, A., Utzinger, U., Vande Geest, J.P.: Microstructural and biomechanical alterations of the human aorta as a function of age and location. Biomechanics and Modeling in Mechanobiology **9**(6), 725–36 (2010). DOI: 10.1007/s10237-010-0209-7.

[13] Holzapfel, G.A., Gasser, T.G., Ogden, R.W.: A new constitutive framework for arterial wall mechanics and a comparative study of material models. Journal of Elasticity **61**, 1–48 (2000)

[14] Holzapfel, G.A., Ogden, R.W.: Constitutive modelling of arteries. Proceedings of the Royal Society A: Mathematical, Physical and Engineering Sciences **466**(2118), 1551–1597 (2010). DOI: 10.1098/rspa.2010.0058.

[15] Humphrey, J.D., Milewicz, D.M., Tellides, G., Schwartz, M.A.: Dysfunctional Mechanosensing in Aneurysms. Science **344**(6183), 477–479 (2014). DOI: 10.1126/science.1253026.

[16] Iliopoulos, D.C., Deveja, R.P., Kritharis, E.P., Perrea, D., Sionis, G.D., Toutouzas, K., Stefanadis, C., Sokolis, D.P.: Regional and directional variations in the mechanical properties of ascending thoracic aortic aneurysms. Medical Engineering & Physics **31**, 1–9 (2009). DOI: 10.1016/j.medengphy.2008.03.002

[17] Iliopoulos, D.C., Kritharis, E.P., Giagini, A.T., Papadodima, S.A., Sokolis, D.P.: Ascending thoracic aortic aneurysms are associated with compositional remodeling and vessel stiffening but not weakening in age-matched subjects. The Journal of Thoracic and Cardiovascular Surgery **137**, 101–109 (2009). DOI: 10.1016/j.jtcvs.2008.07.023.

[18] Juvonen, T., Ergin, M.A., Galla, J.D., Lansman, S.L., Nguyen, K.H., Mccullough, J.N., Levy, D., de Asla, R.A., Bodian, C.A., Griepp, R.B.: Prospective Study of the Natural History of Thoracic Aortic Aneurysms. Annals of Thoracic Surgery **4975**(97), 1533–45 (1997)

[19] Khanafer, K., Duprey, A., Zainal, M., Schlicht, M., Williams, D., Berguer, R.: Determination of the elastic modulus of ascending thoracic aortic aneurysm at different ranges of pressure using uniaxial tensile testing. The Journal of Thoracic and Cardiovascular Surgery **142**(3), 682–686 (2011). DOI: 10.1016/j.jtcvs.2010.09.068.

[20] Koullias, G.J., Ravichandran, P., Korkolis, D.P., Rimm, D.L., Elefteriades, J.A.: Increased tissue microarray matrix metalloproteinase expression favors proteolysis in thoracic aortic aneurysms and dissections. The Annals of Thoracic Surgery **78**(6), 2106–10 (2004). DOI: 10.1016/j.athoracsur.2004.05.088.

[21] Lu, J., Zhao, X.F.: Pointwise Identification of Elastic Properties in Nonlinear Hyperelastic Membranes-Part I: Theoretical and Computational Developments. Journal of Applied Mechanics -Transactions of the ASME **76**(6), 061,013/1–061,013/10 (2009). DOI: 10.1115/1.3130805.

[22] Lu, J., Zhou, X.L., Raghavan, M.L.: Inverse method of stress analysis for cerebral aneurysms. Biomechanics and Modeling in Mechanobiology **7**(6), 477–86 (2008). DOI: 10.1007/s10237-007-0110-1.

[23] Miller, K., Lu, J.: On the prospect of patient-specific biomechanics without patient-specific properties of tissues. Journal of the mechanical behavior of biomedical materials **27**, 154–166 (2013). DOI: 10.1016/j.jmbbm.2013.01.013.

[24] O'Leary, S.A., Doyle, B.J., McGloughlin, T.M.: Comparison of methods used to measure the thickness of soft tissues and their influence on the evaluation of tensile stress. Journal of Biomechanics **46**(11), 1955–60 (2013). DOI: 10.1016/j.jbiomech.2013.05.003.

[25] Raghavan, M.L., Kratzberg, J., Castro de Tolosa, E.M.a., Hanaoka, M.M., Walker, P., da Silva, E.S.a.: Regional distri-

bution of wall thickness and failure properties of human abdominal aortic aneurysm. Journal of Biomechanics **39**(16), 3010–6 (2006). DOI: 10.1016/j.jbiomech.2005.10.021.

[26] Romo, A., Badel, P., Duprey, A., Favre, J.P., Avril, S.: In vitro analysis of localized aneurysm rupture. Journal of Biomechanics **47**(3), 607–616 (2014)

[27] Schlatmann, T., Becker, A.: Histologic Changes in the Normal Aging Aorta : Implications for Dissecting Aortic Aneurysm. American Journal of Cardiology **39**(January), 13–20 (1977)

[28] Schriefl, A.J., Reinisch, A.J., Sankaran, S., Pierce, D.M., Holzapfel, G.A.: Quantitative assessment of collagen fibre orientations from two-dimensional images of soft biological tissues. Journal of the Royal Society - Interface **9**(76), 3081–3093 (2012). DOI: 10.1098/rsif.2012.0339

[29] Sherebrin, M.H., Hegney, J.E., Roach, M.R.: Effects of age on the anisotropy of the descending human thoracic aorta determined by uniaxial tensile testing and digestion by NaOH under load. Canadien Journal of Physiology and Pharmacology **67**, 871–878 (1989)

[30] Simo, J., Pister, K.: Remarks on rate constitutive equations for finite deformation problems: computational implications. Computer Methods in Applied Mechanics and Engineering **46**(2), 201–215 (1984). DOI: 10.1016/0045-7825(84)90062-8.

[31] Tang, P.C.Y., Coady, M.A., Lovoulos, C., Dardik, A., Aslan, M., Elefteriades, J.A., Tellides, G.: Hyperplastic cellular remodeling of the media in ascending thoracic aortic aneurysms. Circulation **112**(8), 1098–105 (2005). DOI: 10.1161/circulationaha.104.511717.

[32] Tonge, T.K., Voo, L.M., Nguyen, T.D.: Full-field bulge test for planar anisotropic tissues: part II–a thin shell method for determining material parameters and comparison of two distributed fiber modeling approaches. Acta Biomaterialia **9**(4), 5926–42 (2013). DOI: 10.1016/j.actbio.2012.11.034.

[33] Trabelsi, O., Davis, F.M., Rodriguez-Matas, J.F., Duprey, A., Avril, S.: Patient specific stress and rupture analysis of ascending thoracic aneurysms. Journal of Biomechanics (2015). DOI: 10.1016/j.jbiomech.2015.04.035.

[34] Wilson, J.S., Baek, S., Humphrey, J.D.: Importance of initial aortic properties on the evolving regional anisotropy , stiffness and wall thickness of human abdominal aortic aneurysms Importance of initial aortic properties on the evolving regional anisotropy , stiffness and wall thickness of hu. Journal of the Royal Society Interface **9**, 2047–2058 (2012). DOI: 10.1098/rsif.2012.0097

[35] Zhao, X.F., Chen, X.L., Lu, J.: Pointwise Identification of Elastic Properties in Nonlinear Hyperelastic Membranes-Part II: Experimental Validation. Journal of Applied Mechanics -Transactions of the ASME **76**(6), 061,014/1–061,014/8 (2009). DOI: 10.1115/1.3130810.
@articleLu2009a, Lu, J., Zhao, X.F.: Pointwise Identification of Elastic Properties in Nonlinear Hyperelastic Membranes-Part I Theoretical and Computational Developments. Journal of Applied Mechanics -Transactions of the ASME **76**(6), 061013/1–061013/10 (2009). DOI: 10.1115/1.3130810.

[36] Zhao, X.F., Chen, X.L., Lu, J.: Pointwise Identification of Elastic Properties in Nonlinear Hyperelastic Membranes-Part II: Experimental Validation. Journal of Applied Mechanics -Transactions of the ASME **76**(6), 061,014/1–061,014/8 (2009). DOI: 10.1115/1.3130810.

[37] Zhao, X.F., Raghavan, M.L., Lu, J.: Characterizing heterogeneous elastic properties of cerebral aneurysms with unknown stress-free geometry a precursor to in vivo identification. Journal of Biomechanical Engineering -Transactions of the ASME, **133**(5), 051,008/1–051,008/12 (2011)

Tables

r

Table 1: Patient demographics for the study population

Patient	Gender	Age	Diameter (mm)
1	F	80	52
2	M	79	52
3	M	76	58
4	M	72	51
5	F	76	65
6	M	55	55

Table 2: Magnitude of the wall tension and strain at the highest pressure prior to rupture

Patient	Pressure	Wall Tension (N/mm)		Strain	
	(kPa)	Max	Mean ± S.D.	Max	Mean ± S.D.
1 (a)	57	0.94	0.74±0.10	0.28	0.22±0.02
(b)	87	1.43	1.17±0.14	0.35	0.30±0.03
2	96	1.51	1.14±0.15	0.33	0.27±0.03
3 (a)	48	0.82	0.56±0.08	0.44	0.34±0.03
(b)	42	0.90	0.57±0.12	0.23	0.16±0.03
4 (a)	78	1.57	1.01±0.14	0.44	0.31±0.03
(b)	42	0.69	0.50±0.05	0.27	0.18±0.03
5	81	2.06	1.02±0.27	0.43	0.26±0.06
6 (a)	117	2.05	1.34±0.22	0.95	0.80±0.06
(b)	96	1.64	1.05±0.18	0.87	0.64±0.04

Table 3: Descriptive statistics for the material property distributions shown in Figs. 6 and 7.

		Mean	Median	Std Dev	Skewness	Kurtosis
1 (b)	μ_1	0.0028	0	0.0074	4.1386	23.7033
	μ_2	0.7123	0.7351	0.2453	0.0156	2.7712
	γ	12.0604	11.1882	3.0158	0.9773	3.8401
	κ	0.3958	0.3886	0.0299	0.8307	3.4212
	θ	0.5365	0.4032	0.5321	3.3065	14.4633
4 (b)	μ_1	0.0018	0	0.0043	3.4680	18.5121
	μ_2	1.4084	1.3704	0.2974	1.5814	7.4487
	γ	12.7826	11.8353	6.0428	0.5562	2.7954
	κ	0.4462	0.4521	0.0322	-1.2805	5.0428
	θ	1.5451	1.4854	0.8418	0.1168	1.9919
6 (a)	μ_1	0.0066	0.0010	0.0175	6.4364	54.8773
	μ_2	0.2770	0.2807	0.0553	1.2496	20.4054
	γ	2.1980	2.1277	0.4616	0.7771	5.8666
	κ	0.4217	0.4346	0.0650	-2.5316	13.7902
	θ	1.5495	1.5272	1.0283	0.0627	1.6067
6 (b)	μ_1	0.0122	0.0040	0.0188	3.9096	35.9472
	μ_2	0.2672	0.2531	0.1229	2.1150	14.0472
	γ	1.6037	1.5061	0.5736	1.4399	7.5616
	κ	0.4078	0.4205	0.0594	-1.2877	5.6325
	θ	1.5440	1.5203	0.8567	0.1441	2.0727

Table 4: Comparison of the magnitude of the displacement, strain, and wall tension from the experimental measurements with the forward finite element predictions

Patient	Pressure (kPa)	Percent Error in		
		Wall tension	Strain	Displacement
1 (a)	57	2.50	1.50	0.12
(b)	87	5.86	4.89	0.95
2	96	1.73	1.30	0.22
3(a)	48	2.94	7.61	0.64
(b)	42	3.83	6.01	0.49
4(a)	72	3.52	2.56	0.26
(b)	42	2.29	3.87	0.71
5	81	3.64	3.84	0.36
6(a)	117	4.95	1.36	0.14
(b)	96	3.46	0.81	0.16

Table 5: Descriptive statistics for the material property distributions. Note that the measures for Patient 1b, 4b, 6a and 6b are given in Table 3.

		Mean	Median	Std Dev	Skewness	Kurtosis
1 (a)	μ_1	0.0047	0.0012	0.0090	3.7921	19.5557
	μ_2	1.1165	1.1502	0.2054	-0.1503	2.7491
	γ	13.7068	13.4217	3.0240	0.4603	5.0969
	κ	0.4233	0.4262	0.0331	-1.8461	19.9887
	θ	1.8882	2.2175	1.2097	-0.3925	1.4855
2	μ_1	0.0017	0	0.0060	4.5407	26.1463
	μ_2	0.7166	0.7652	0.2630	0.3218	7.5274
	γ	9.8319	10.3928	4.5851	-0.4299	2.6246
	κ	0.4230	0.4318	0.0522	-1.9860	11.9698
	θ	1.3945	1.2512	0.9535	0.3937	1.8862
3 (a)	μ_1	0.0022	0	0.0044	2.7460	11.6565
	μ_2	0.2758	0.2749	0.0786	0.3751	2.5502
	γ	7.8431	7.6124	2.5195	1.3931	9.6512
	κ	0.4185	0.4248	0.0419	-0.7713	3.7932
	θ	1.3099	1.1941	0.8443	0.5395	2.4616
3 (b)	μ_1	0.0113	0.0009	0.0196	3.0088	15.2960
	μ_2	1.7624	1.4787	1.3935	2.4358	11.4874
	γ	26.9275	21.5273	20.2774	1.7354	6.3912
	κ	0.3464	0.3695	0.1029	-1.4226	5.3000
	θ	1.6516	1.8058	0.8855	-0.2391	1.9042
4 (a)	μ_1	0.0065	0	0.0127	4.1308	30.2357
	μ_2	1.0477	1.0526	0.2883	0.9123	8.4815
	γ	6.2818	6.6803	2.2482	0.7771	5.8666
	κ	0.4169	0.4203	0.0362	-1.3506	8.6815
	θ	1.1482	0.6286	1.1126	0.7589	1.9070
5	μ_1	0.0056	0	0.0205	7.7152	73.2692
	μ_2	1.1530	0.9998	0.7542	0.9761	3.6953
	γ	15.4332	12.9441	8.1854	4.6660	43.4995
	κ	0.3711	0.3907	0.0905	-1.6403	6.8814
	θ	1.7388	1.7403	0.8125	-0.1929	2.2813

Figures

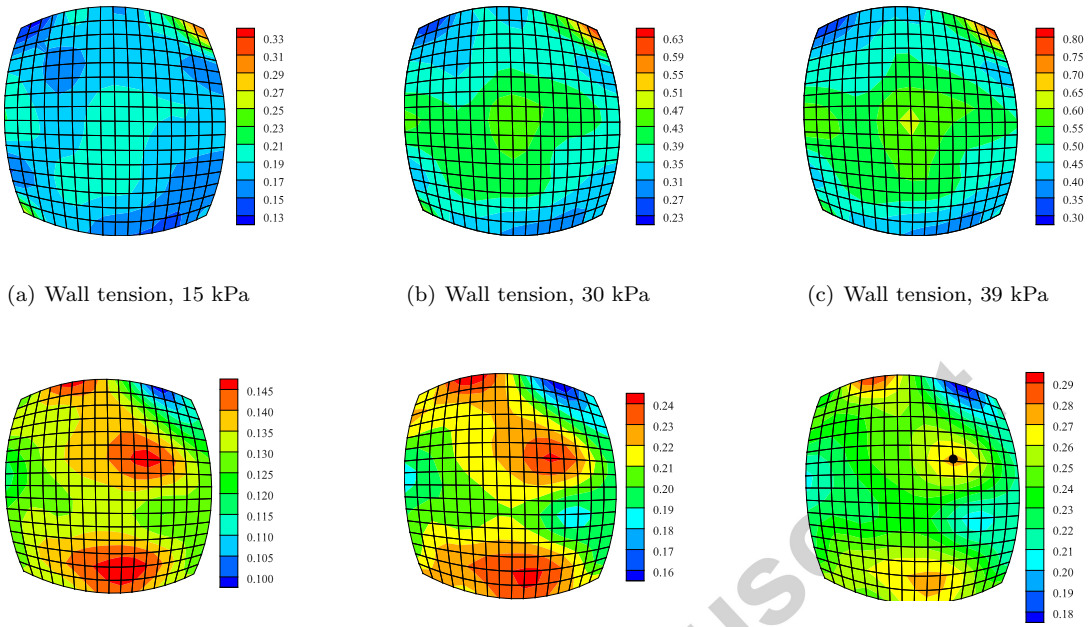

(a) Wall tension, 15 kPa (b) Wall tension, 30 kPa (c) Wall tension, 39 kPa

(d) Strain, 15 kPa (e) Strain, 30 kPa (f) Strain, 39 kPa

Figure 1: Magnitude of the (a-c) wall tension and (d-f) strain for Patient 3a at pressures of (a,d) 15, (b, e) 30, and (c, f) 39 kPa. The black dot in (f) denotes the rupture location.

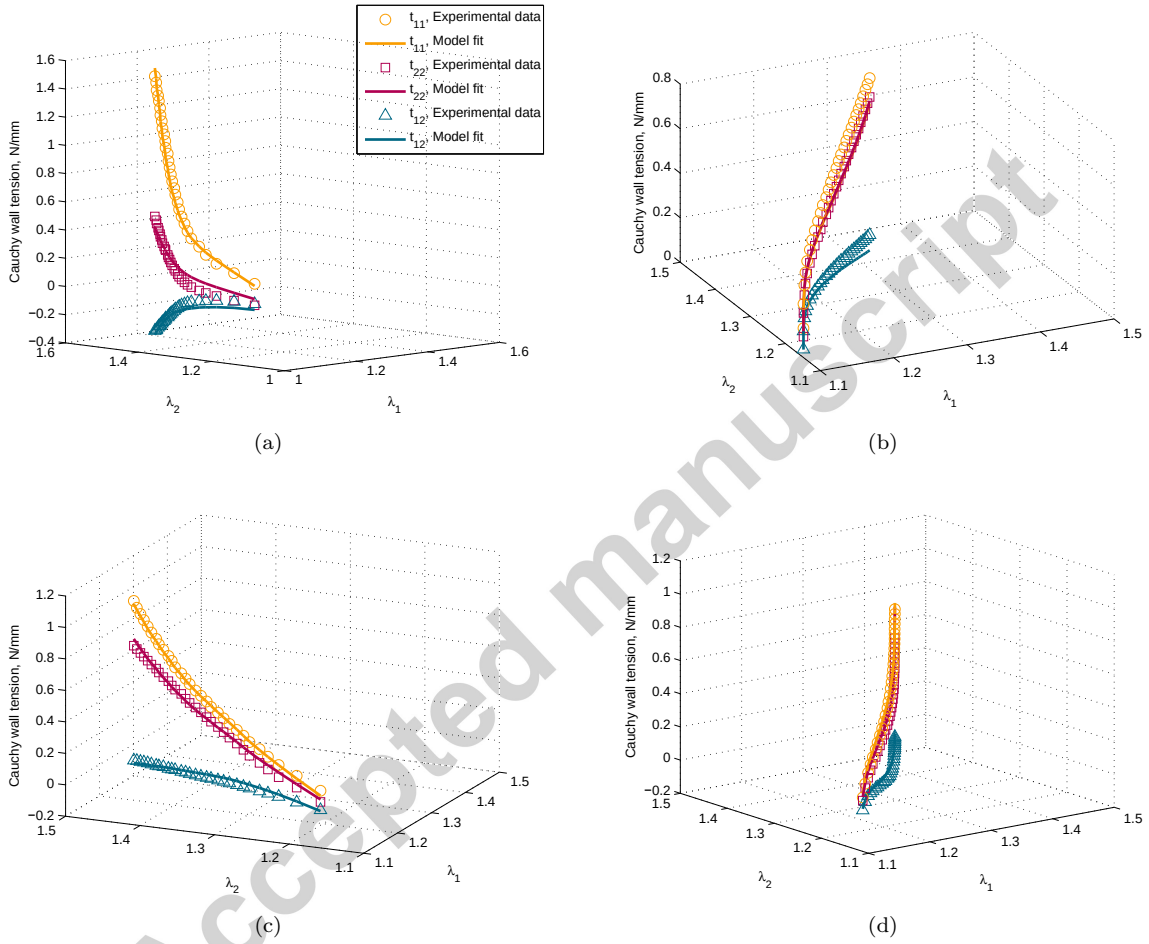

Figure 2: Local wall tension versus stretch curves at four different locations for Patient 2. Note that the curves have been rotated into their principal strain state to facilitate plotting.

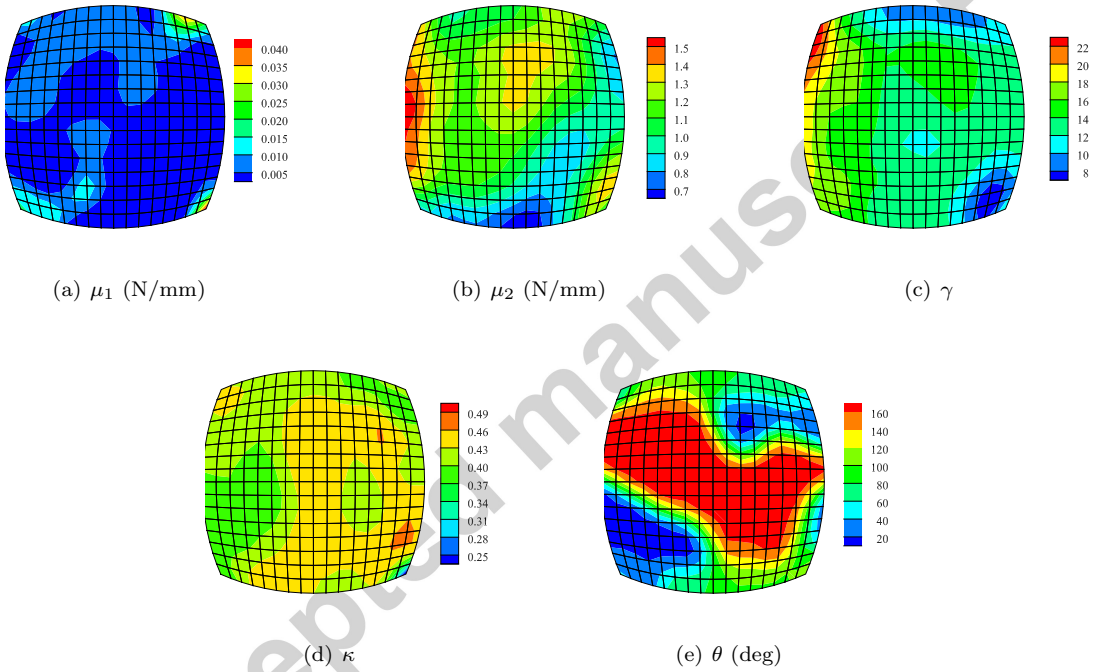

(a) μ_1 (N/mm) (b) μ_2 (N/mm) (c) γ

(d) κ (e) θ (deg)

Figure 3: Distribution of the identified material parameters over the ATAA for Patient 1a.

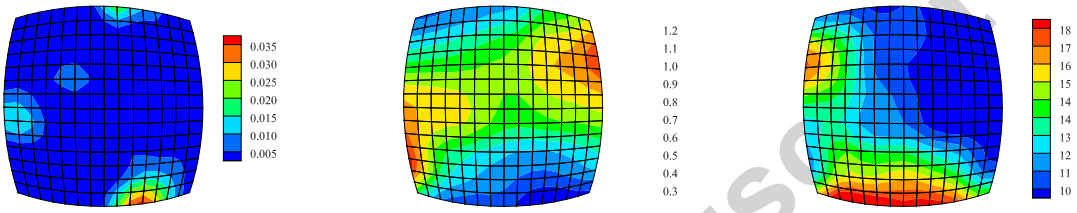

(a) μ_1 (N/mm) (b) μ_2 (N/mm) (c) γ

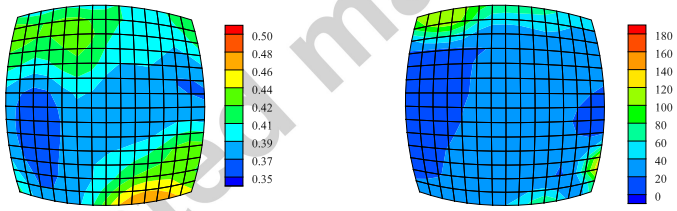

(d) κ (e) θ (deg)

Figure 4: Distribution of the identified material parameters over the ATAA for Patient 1b.

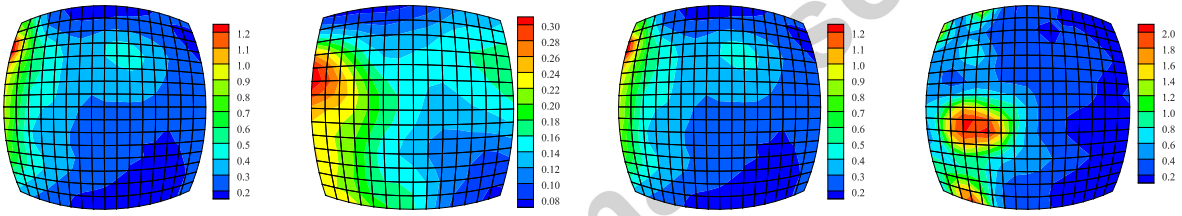

(a) Patient 1a (b) Patient 1b (c) Patient 4a (d) Patient 4b

Figure 5: Maps of the strain energy calculated from Eq. 1 for a uniform equibiaxial stretch of 1.2 using the pointwise material properties for (a) Patient 1a, (b) Patient 1b, (c) Patient 4a, and (d) Patient 4b.

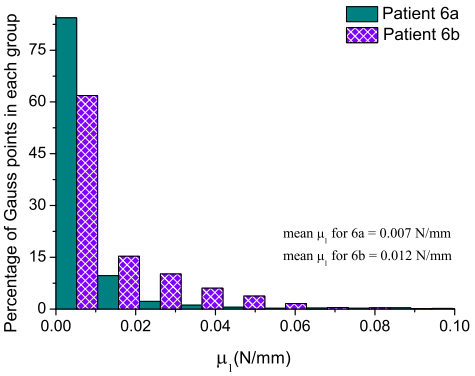

(a)

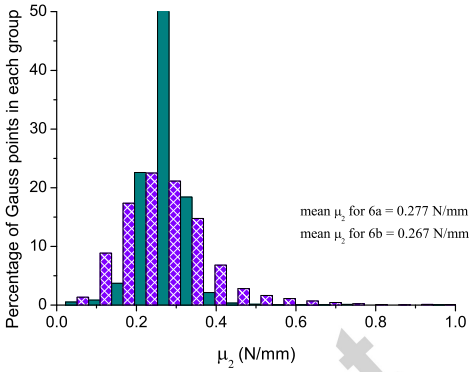

(b)

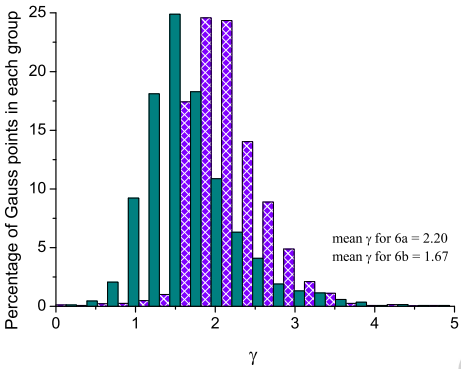

(c)

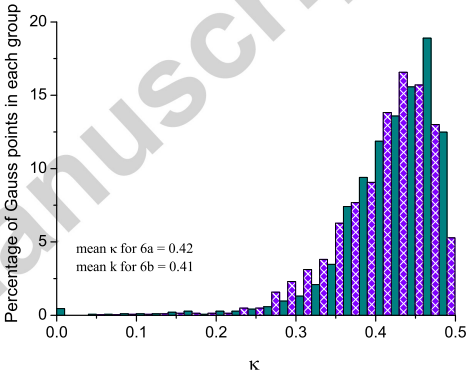

(d)

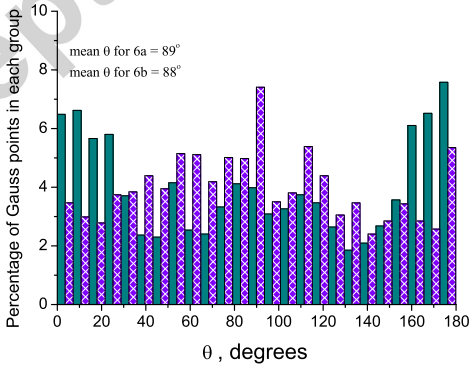

(e)

Figure 6: Histograms of the identified material parameters over the ATAA for Patient 6.

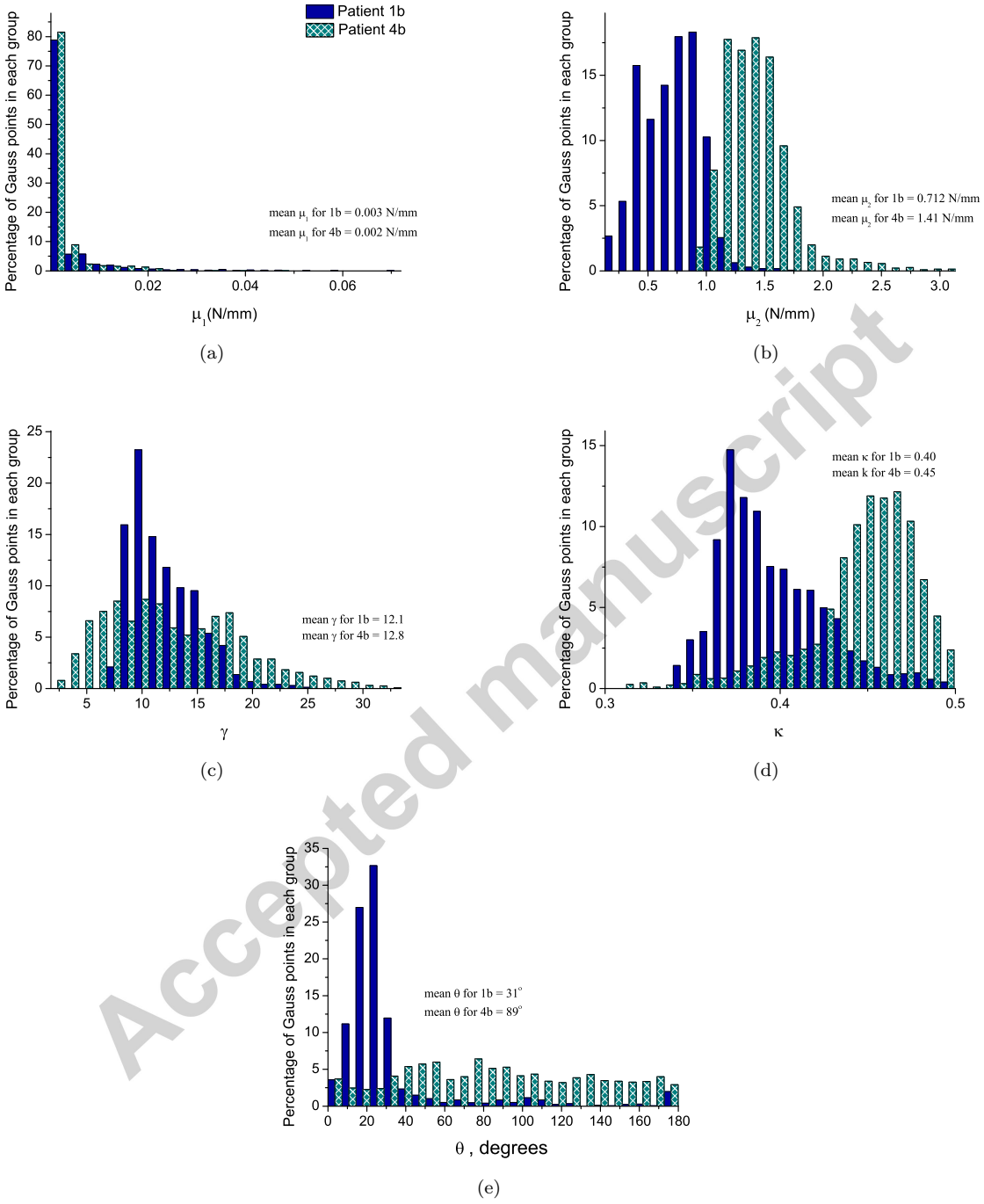

Figure 7: Histograms of the identified material parameters over the ATAA for Patient 1b (solid blue) and 4b (green diagonal cross hatch).

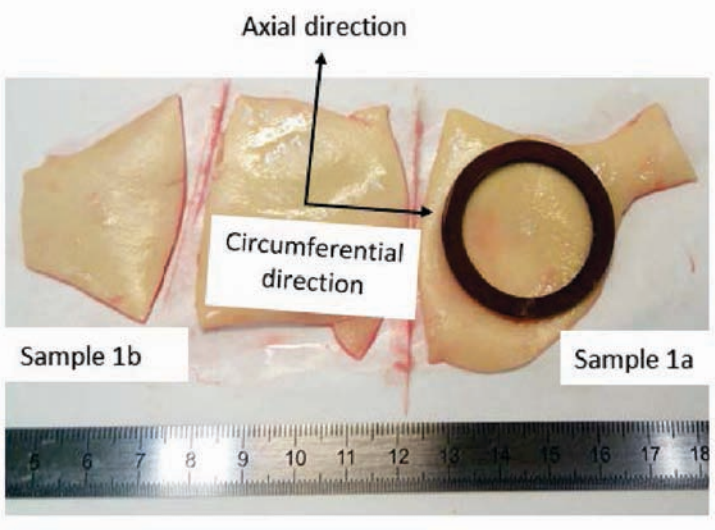

Figure 8: Location of the two samples collected from Patient 1 with the axial and circumferential directions marked. The fixture shown on Sample 1a indicates the region of tissue that would be mounted in the bulge inflation device.

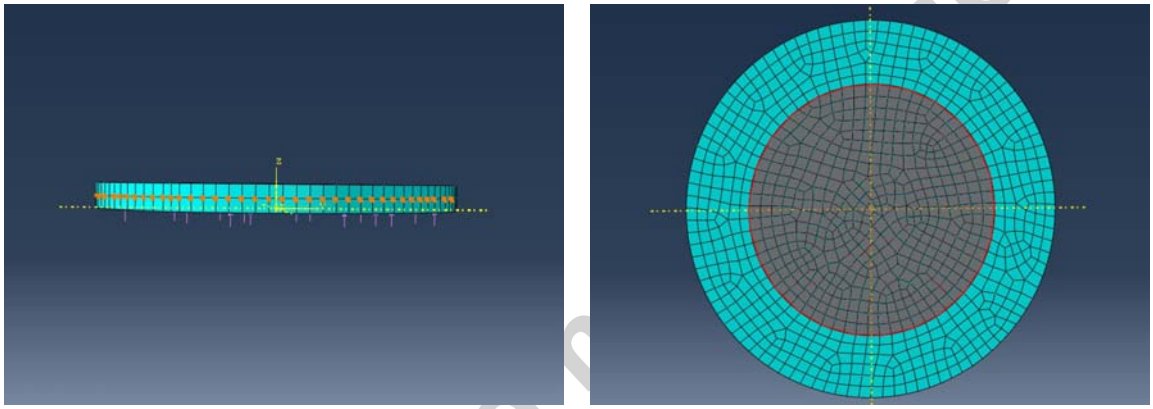

(a) (b)

Figure 9: ABAQUS model. (a) Side view of the model showing pressure loading and fixed boundary condition at the plate mid-line. (b) Top view of the model. The elements in grey were used in the inverse analysis.

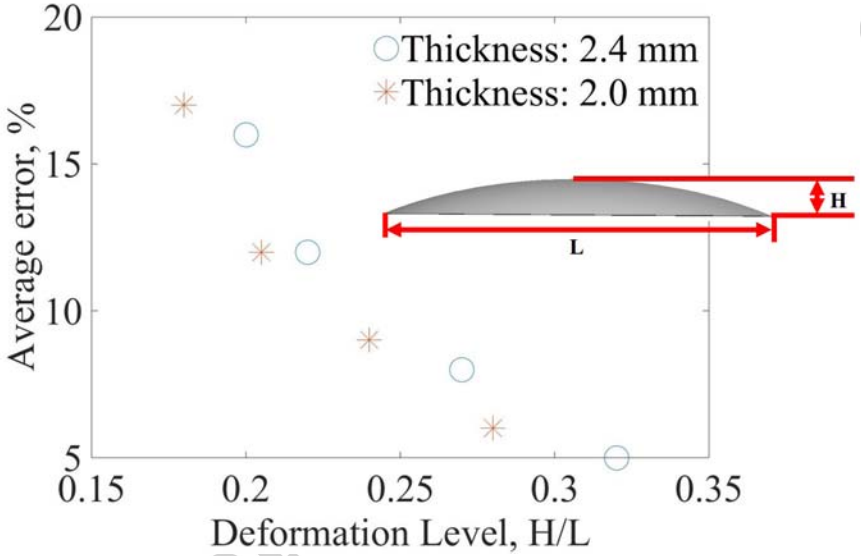

Figure 10: Percent error in P_1 versus the deformation level measured by the ratio of the out-of-plane displacement to the specimen diameter.

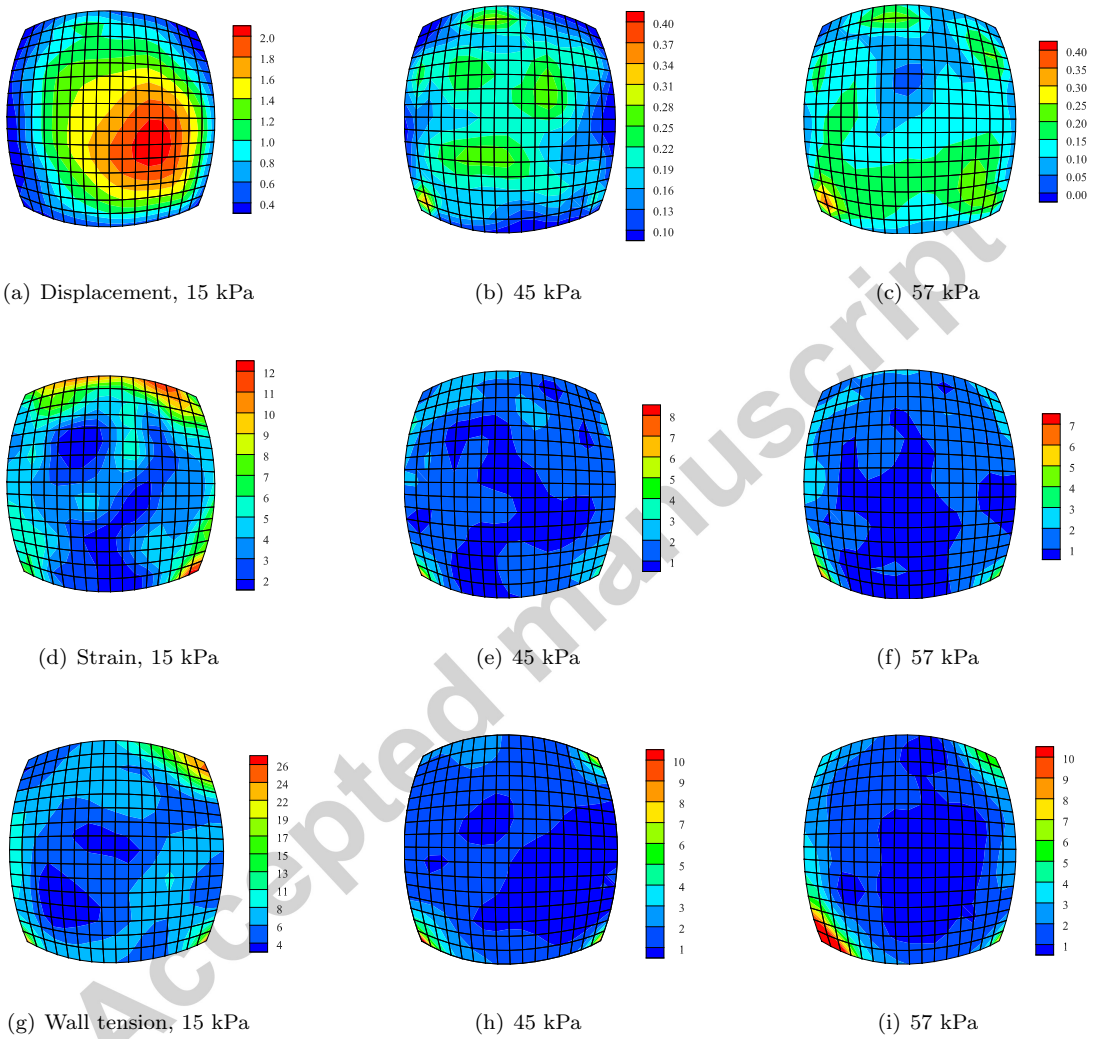

(a) Displacement, 15 kPa (b) 45 kPa (c) 57 kPa

(d) Strain, 15 kPa (e) 45 kPa (f) 57 kPa

(g) Wall tension, 15 kPa (h) 45 kPa (i) 57 kPa

Figure 11: Percentage error between the (a-c) measured displacement, (d-f) DIC computed strains, and (g-i) computed wall tension and the displacement, strain and wall tension predicted from the forward finite element analysis, respectively. The results are presented Patient 1a at (a,d,g) 15 kPa, (b,e,h) 45 kPa, and (c,f,i) 57 kPa.